Three-dimensional structure of confined swirling jets at moderately large Reynolds numbers

E. Sanmiguel-Rojas,[1] M. A. Burgos,[2] C. del Pino,[3] and R. Fernandez-Feria[3]
[1]*Escuela Politécnica Superior, Universidad de Jaén, 23071 Jaén, Spain*
[2]*E.T.S.I. Industriales, Universidad Pol. de Cartagena, 30202 Cartagena, Spain*
[3]*E.T.S. Ingenieros Industriales, Universidad de Málaga, 29013 Málaga, Spain*

(Received 10 September 2007; accepted 4 March 2008; published online 21 April 2008)

We have performed a series of three-dimensional (3D) numerical simulations of the incompressible flow discharging from a rotating pipe into a coaxial static cylindrical container through a sudden expansion. We have considered several values of the Reynolds number based on the pipe flow rate Re_Q between 50 and 300, and an expansion diameter ratio of 8, and have analyzed the emerging 3D flow structures in the swirling jet exiting from the rotating pipe as the swirl parameter S is increased. The results are compared to axisymmetric numerical simulations of the same problem. Three-dimensional, nonlinear instabilities are found in the swirling jet when $\mathrm{Re}_Q \gtrsim 98$ above a critical value of S, which depends on Re_Q, that obviously do not appear in the axisymmetric simulations. These nonlinear instabilities are initially triggered by the linear instabilities inside the rotating pipe, which are already present in the pipe from a much lower value of S, and are transformed in the jet. As S increases further, there exists another critical value above which the swirling jet undergoes vortex breakdown, producing a flow in the jet which is basically axisymmetric. This critical value of the swirl parameter for breakdown is significantly larger than that found in the axisymmetric simulations. Thus, one of the main results of the present work is that 3D instabilities delay the formation of vortex breakdown in the jet, in relation to the same axisymmetric flow, but once the vortex breakdown phenomenon occurs, the 3D instabilities coming from the rotating pipe appear to be suppressed in the jet, and the swirling flow becomes basically axisymmetric again. Finally, the axisymmetric simulations show that the jet becomes unstable to axisymmetric perturbations, when $\mathrm{Re}_Q \gtrsim 188$, above another critical value of S. However, these axisymmetric instabilities do not appear in the 3D simulations because the flow becomes unstable to asymmetric perturbations at much lower values of S. © *2008 American Institute of Physics*.
[DOI: 10.1063/1.2907218]

I. INTRODUCTION

Confined swirling jets are of interest in several technical and industrial applications.[1] For instance, they are important in combustion systems to enhance mixing, reduce pollution, and for flame stabilization by taking advantage of the vortex breakdown phenomenon.[2,3] The knowledge and detailed characterization of the different structures appearing in the flow as the governing parameters are varied due to linear and nonlinear instabilities, and to other phenomena such as vortex breakdown, is crucial for the implementation of these practical applications of swirling jets.

The structure of an *axisymmetric* swirling jet in a sudden expansion pipe has been recently considered theoretically and numerically by Revuelta *et al.*[4–6] In particular, Revuelta[6] characterized the critical swirl parameter (S^*) for the onset of vortex breakdown by numerically solving the axisymmetric Navier–Stokes equations for several values of the pipe diameter expansion ratio δ^{-1} and for moderately large Reynolds numbers Re_Q for which the flow remains laminar (see next section for the definition of the dimensionless parameters). For given Re_Q and δ^{-1}, when the swirl parameter S is larger than a critical value S^*, a stagnation point is formed in the axis of the flow at a certain distance from the entrance of the jet, generating the typical axisymmetric "vortex breakdown bubble" structure. For sufficiently large Reynolds numbers and expansion ratios, the vortex breakdown bubble structure appears as a fold above S^* in the solution space of a suitable chosen variable versus S, for a given Re_Q. This overall behavior is qualitatively similar to that previously found in axisymmetric swirling flows in pipes.[7–10] In addition, an oscillatory behavior of the axisymmetric flow was found in Ref. 6 above another critical swirl number for sufficiently large values of Re_Q and expansion ratios.

Three-dimensional (3D) numerical simulations of unconfined swirling jets were recently performed by Ruith *et al.*[11] by using a Grabowski and Berger[12] vortex model at the flow inlet. After the formation of the axisymmetric vortex breakdown bubble above a critical value of the swirl number for a given Re_Q, helical disturbances may appear at the wake of the main breakdown bubble if Re_Q is large enough, leading to helical breakdown modes. Similar results, but for a swirling jet confined inside a pipe and using a q-vortex model at the inlet, were recently reported in Ref. 13. These standing helical waves are shown to be originated from absolute instabilities located inside the axisymmetric breakdown bubble.[13,14] Both inlet vortex models are quite similar to each other in that there exists a central core where the

TABLE I. Critical swirl numbers for convective instabilities in the rotating Hagen–Poiseuille flow (S_{ci}), taken from Ref. 21, and for axisymmetric vortex breakdown (S_{2Dvb}), for the Reynolds numbers considered in Sec. III.

Re_Q	100	150	200
S_{ci}	0.46	0.20	0.14
S_{2Dvb}	0.995	0.9675	1.005

azimuthal velocity behaves as a solid body rotation near the axis and then decays radially as a potential vortex outside the core. This, together with the fact that in the confined case[13] the pipe radius is about four times the size of the vortex core, explains why the results were qualitatively similar in both cases.

In the present work, we discuss results from 3D numerical simulations of a swirling jet in a quite different configuration, with a rotating pipe flow as the initial condition of the jet. In particular, we consider the discharge of a rotating pipe into another nonrotating pipe of a much larger radius through a sudden expansion (we have selected an expansion diameter ratio of $\delta^{-1}=8$ in our numerical simulations) at moderately large values of Re_Q (Re_Q between 50 and 300) for which the flow remains laminar. This configuration allows for a very precise specification of the upstream boundary conditions of the incoming swirling jet and, more importantly, it should be possible to experimentally reproduce the results in exactly the same configuration. We find that the behavior of the swirling jet, as the swirl parameter S is increased for a given Re_Q, is qualitatively different to both the axisymmetric simulations and the 3D numerical simulations for a Gaussian-like vortex at the inlet just mentioned.[11,13] First, the rotating pipe flow becomes linearly unstable to helical disturbances for relatively low values of the swirl parameter (for a given Reynolds number). These centrifugal instabilities are captured by our numerical method from just numerical noise,[15] without any artificial forcing. As a consequence, the discharging swirling jet is nonaxisymmetric for swirl numbers well below the critical value for vortex breakdown. Second, the critical swirl for vortex breakdown is significantly larger than that predicted by the axisymmetric simulations for the same expansion ratio and Re_Q owing to the presence of these 3D instabilities. The resulting vortex breakdown structures are always 3D, in contrast to previous 3D results,[11,13] since the flow becomes unstable to helical disturbances long before undergoing an axisymmetric vortex breakdown transition. However, we shall see that the vortex breakdown tends to suppress the helical waves coming from the rotating pipe, with the consequence that the swirling jet becomes *almost* axisymmetric after vortex breakdown.

In order to compare to the axisymmetric [two dimensional (2D) for short] behavior, we have also performed axisymmetric numerical simulations for exactly the same configurations considered in the 3D simulations and using the same numerical code. Finally, it is worth mentioning that the type of swirling jet issued from a rotating pipe studied here has been recently considered by Facciolo *et al.*,[16,17] both experimentally and numerically, but for quite large Reynolds numbers (larger than 10^4), for which the flow is *turbulent.*

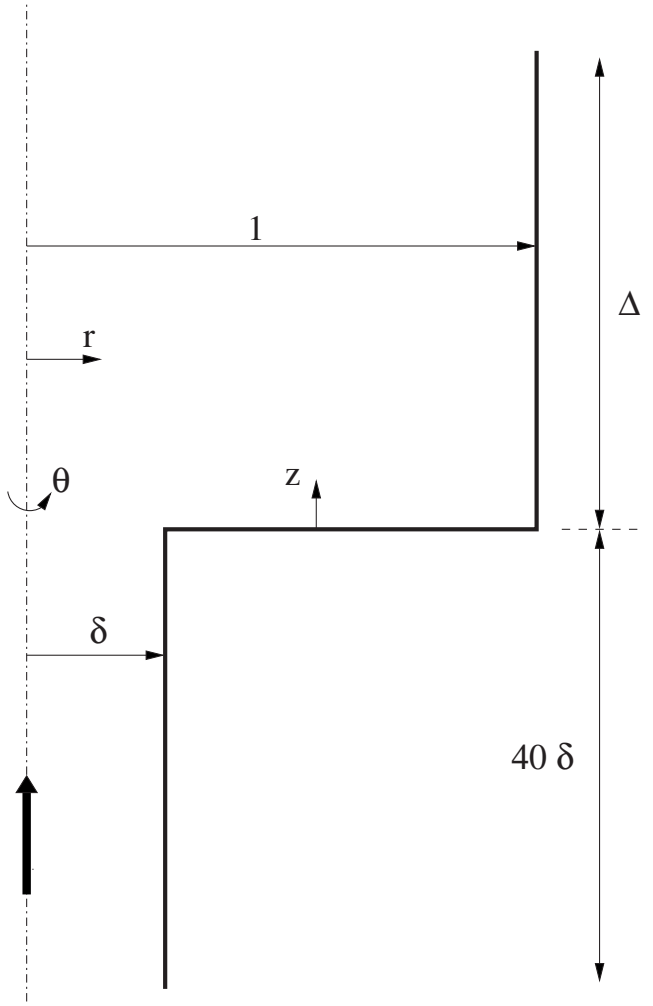

FIG. 1. Sketch of the nondimensional integration domain and coordinates. The bold arrow shows the direction of the incoming flow from the rotating pipe with radius δ (we use $\delta=0.125$ in the computations). The cylinder with larger (unity) radius is nonrotating.

Therefore, their results cannot be directly compared to our present results for a swirling laminar jet in a sudden expansion. The main aim of the present work is to understand and characterize with precision the 3D *laminar* flow transitions taking place at moderately large Reynolds numbers (of the order of a few hundreds). As commented above, this knowledge is of interest in several technical and industrial applications where swirling jets are used.

II. FORMULATION OF THE PROBLEM AND NUMERICAL METHOD

We numerically solve the 3D, incompressible Navier–Stokes equations, which in dimensionless form can be written as

$$\nabla \cdot \mathbf{v} = 0, \tag{1}$$

$$\frac{\partial \mathbf{v}}{\partial t} + \mathbf{v} \cdot \nabla \mathbf{v} = -\nabla p + \frac{1}{\mathrm{Re}} \nabla^2 \mathbf{v}, \tag{2}$$

in the domain depicted in Fig. 1, which consists of a rotating pipe of (dimensional) length l and (dimensional) diameter d

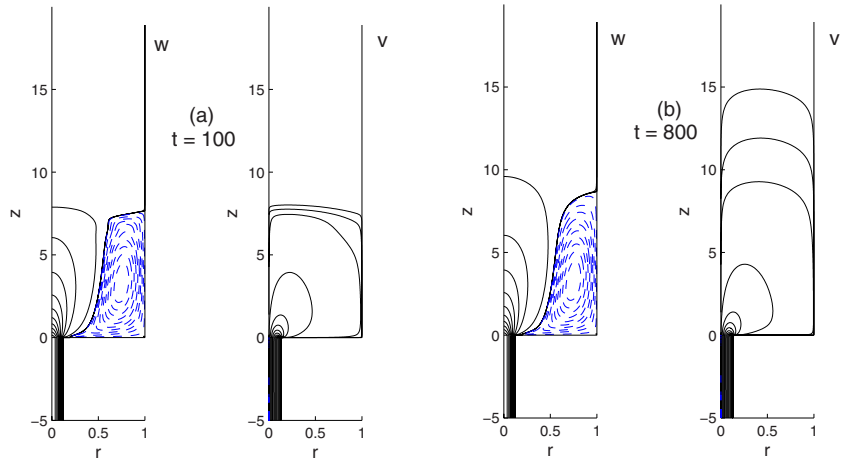

FIG. 2. (Color online) Contour lines of the axial velocity w and the azimuthal velocity v (as indicated) in the axial plane $\theta=0$ for $\mathrm{Re}_Q=100$, $S=0.5$, and two instants of time, $t=100$ (a) and $t=800$ (b). For each variable we plot ten equidistant contour lines between 0 and the maximum value in the domain with continuous lines, and ten equidistant contour lines between 0 and the minimum (negative) value in the domain with dashed lines (if that is the case). w ranges between −0.022 and 0.84, and v between 0 and 0.41, approximately.

discharging into a coaxial stationary cylindrical tube of radius $R(>d/2)$. This radius R is used as the length scale in the nondimensional notation of Fig. 1 [see also the boundary conditions (5)–(7) below]. We have selected in the computations a pipe length $l=20\times d$ and an expansion diameter ratio δ^{-1} given by

$$\frac{2R}{d}\equiv\frac{1}{\delta}=8. \tag{3}$$

Cylindrical-polar coordinates (r,θ,z), with velocity field $\mathbf{v}=(u,v,w)$, are used. The flow is produced by a (dimensional) pressure difference $(\Delta p)_c$, which includes gravity forces [p in Eq. (2) is the nondimensional *reduced* pressure], between the rotating pipe inlet and the exit of the stationary tube, whose dimensional length is L (we have selected $L/R\equiv\Delta=10$ in most of the reported computations, which has been shown to be large enough for the results to be independent of the boundary condition at the flow exit). Accordingly, we define a characteristic velocity based on this pressure difference, $V_c\equiv\sqrt{(\Delta p)_c/\rho}$, where ρ is the fluid density, which, together with the length scale R, is used to nondimensionalize the equations and boundary conditions. Thus, the Reynolds number Re in Eq. (2) is defined as

$$\mathrm{Re}=\frac{V_cR}{\nu}=\frac{\sqrt{(\Delta p)_c/\rho}R}{\nu}, \tag{4}$$

where ν is the kinematic viscosity of the fluid.

The nondimensional boundary conditions are the following (see Fig. 1): Zero velocity at the solid walls, except at the pipe wall, which rotates with an angular velocity Ω,

$$\mathbf{v}=0 \quad \text{at} \begin{cases} r=1, & 0\leqslant z\leqslant\Delta, \quad \Delta\equiv\dfrac{L}{R}, \\ \delta\leqslant r\leqslant 1, & z=0, \qquad \delta\equiv\dfrac{d}{2R}, \end{cases} \tag{5}$$

$$\mathbf{v}=\frac{\Omega(d/2)}{V_c}\mathbf{e}_\theta \quad \text{at } r=\delta, \quad -40\delta\leqslant z\leqslant 0, \tag{6}$$

and given pressure at the center of the inlet and outlet sections,

$$p=1 \quad \text{at } r=0, \quad z=-40\delta$$

and

$$p=0 \quad \text{at } r=0, \quad z=\Delta. \tag{7}$$

We will start the computations with the fluid at rest ($\mathbf{v}=0$ at $t=0$), except otherwise specified. The pressure difference between the inlet section at $z=-40\delta$ and the pipe outlet, $z=\Delta$, sets the fluid into motion without any other constraint on these sections, so that the fluid velocity freely evolves downstream, including the pipe outlet. For details on the numerical technique, see Refs. 15 and 18. In the computations we have used a nonuniform grid in the meridional (r,z)-plane[19] with, typically, $n_r=205\times n_z=377$ nodes concentrated near the pipe exit ($z=0$, $0\leqslant r\leqslant\delta$). Second-order finite differences both in the (r,z)-plane and in time t are used, with a time step $\delta t=5\times10^{-4}$. For the discretization of the azimuthal coordinate θ, we use an eighth-order finite-difference scheme, which is very accurate and efficient with

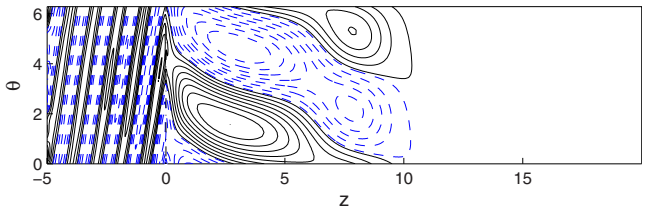

FIG. 3. (Color online) Contour lines of the 3D disturbances $v(0.1,\theta,z)-v(0.1,0,z)$ on the cylindrical surface $r=0.1$ for $\mathrm{Re}_Q=100$ and $S=0.5$ at $t=800$. We plot eight positive values of the contour lines with continuous lines and eight negative values with dashed lines. The contour values ranges between -2.38×10^{-9} and 2.7×10^{-9}. The rotating pipe exit ($z=0$) is marked with a dash-and-dot line.

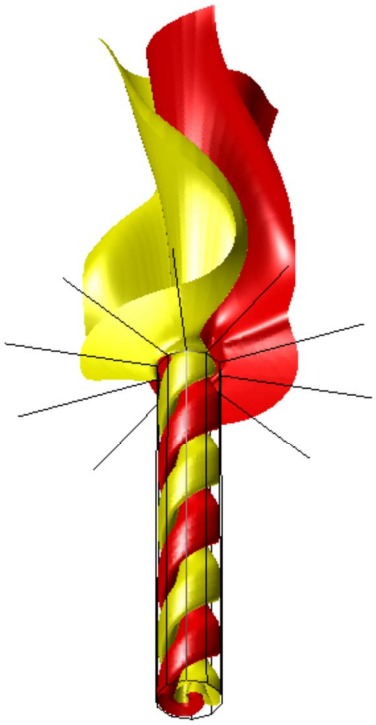

FIG. 4. (Color online) 3D view of the isosurfaces $v-v(\theta=0)=0.25\times10^{-9}$ (dark gray) and $v-v(\theta=0)=-0.25\times10^{-9}$ (light gray) for $\mathrm{Re}_Q=100$ and $S=0.5$ at $t=800$. The wall of the rotating pipe and the sudden expansion at its exit are marked with several straight lines.

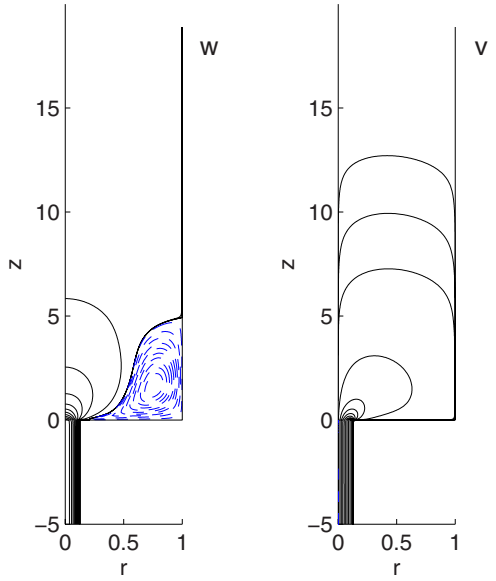

FIG. 5. (Color online) As in Fig. 2 but for $S=0.9$ and $t=700$. w ranges between −0.018 and 0.92 and v between 0 and 0.82, approximately.

just $n_\theta=10$ nodes.[15] In spite of the high accuracy of the eight-order scheme in θ, obviously $n_\theta=10$ would not be enough to disclose structures with azimuthal wave numbers larger than, approximately, 3, for which higher values of n_θ should be used. But this is not the case in the results reported in this paper and, as shown in the Appendix, $n_\theta=10$ yields an excellent accuracy. A typical 3D numerical simulation for a given set of the flow parameters takes between a few days to two weeks in our computer facilities, depending on the Reynolds number.

The accuracy of the numerical method with the above discretization has been assessed in Ref. 15 for the flow in a rotating pipe, reproducing with great precision previous linear stability results[20,21] and capturing the consequent nonlinear traveling waves inside the rotating pipe (nonetheless, a convergence study of the numerical method is given in the Appendix). These centrifugal instabilities in a rotating Hagen–Poiseuille flow have the particularity of being triggered by just numerical noise using our numerical technique, without any other external forcing. In the present work, these linear instabilities generate the necessary perturbations in the inlet (rotating) pipe section to trigger the nonlinear instabilities in the emerging swirling jet after the sudden expansion. Thus, though no external forcing is needed for the development of the swirling jet instabilities reported in the present work, they are actually generated by real perturbations spontaneously appearing inside the upstream rotating pipe (see next section for the details).

Though in the computations, we use the Reynolds number (4) based on the pressure difference, the results given below are presented in terms of the usual Reynolds number based on the flow rate Q, and the pipe diameter d, $\mathrm{Re}_Q=4Q/(\pi d\nu)$. To obtain it, we compute the flow rate at the rotating pipe exit ($z=0$) at each instant of time. In nondimensional form,

$$\mathrm{Re}_q(t)=\mathrm{Re}\,\frac{2}{\pi\delta}\int_0^{2\pi}\int_0^{\delta}[rw]_{z=0}drd\theta. \tag{8}$$

This quantity tends to Re_Q if a steady state is reached at that section,

$$\lim_{t\to\infty}\mathrm{Re}_q(t)=\mathrm{Re}_Q\equiv\frac{4Q}{\pi d\nu}. \tag{9}$$

Numerically, we start with an initial value of Re corresponding to the Hagen–Poiseuille flow rate Q in the rotating pipe ($-40\delta\leqslant z\leqslant 0$), but this value is changed during the computations to reach and to maintain the desired value of Re_Q, which is computed at each time step, using a numerical feedback controller. Once Re for a given Re_Q is thus numerically obtained, we start again the computations with the flow at rest at $t=0$ with this value of Re.

The other nondimensional parameter governing the flow is the swirl number based on the rotation velocity of the pipe and on the flow rate Q,

$$S\equiv\frac{\Omega(d/2)}{W_0},\quad W_0\equiv\frac{8Q}{\pi d^2}. \tag{10}$$

Note that W_0 is the axial velocity at the axis in the developed Hagen–Poseuille in the pipe for the flow rate Q. Alternatively, we may use a rotation-based Reynolds number,

$$\mathrm{Re}_\theta\equiv\frac{\Omega(d/2)^2}{\nu}=S\,\mathrm{Re}_Q. \tag{11}$$

In terms of these nondimensional parameters, the boundary condition (6) for v may be written as

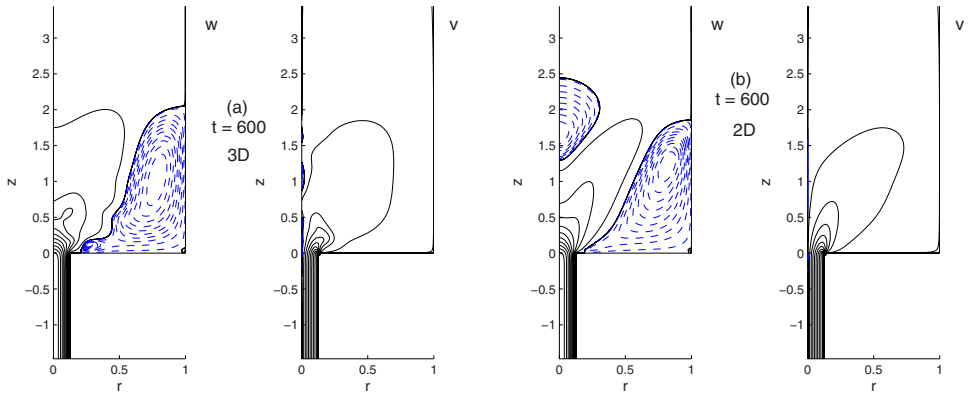

FIG. 6. (Color online) Detail near the pipe exit of the contour lines of w and v (as indicated) in the axial plane $\theta=0$ for $\mathrm{Re}_Q=100$, $S=1$, and $t=600$. In (a) we show the 3D flow, while (b) depicts the axisymmetric analog, containing a clearly visible breakdown bubble on the axis. Contour lines as described in the caption of Fig. 2, with w between −0.018 and 0.94 and v between −0.029 and 0.937 in (a), and w between −0.018 and 0.787 and v between 0 and 0.78 in (b).

$$v = \frac{\mathrm{Re}_\theta}{\mathrm{Re}\ \delta} = \frac{\mathrm{Re}_Q}{\mathrm{Re}}\frac{S}{\delta} \quad \text{at } r=\delta, \quad -40\delta \leqslant z \leqslant 0. \tag{12}$$

The relationship between Re and Re_Q depends on the pressure drop along the flow domain and, therefore, on Re_Q and S for a given δ (=0.125 in the computations reported below). For instance, if $S=1$, $\mathrm{Re}=854$ for $\mathrm{Re}_Q=100$ and $\mathrm{Re}=948$ for $\mathrm{Re}_Q=200$, so that $\mathrm{Re}_Q S/(\mathrm{Re}\delta)$ ranges between 0.9368 and 1.6878, respectively.

III. RESULTS AND DISCUSSION

In this section, we present the results obtained from the 3D simulations for three different values of the Reynolds number, $\mathrm{Re}_Q=100$, 150, and 200, as the swirl parameter S is increased, discussing the different transitions and instabilities taking place in the swirling jet, and remarking the main differences in relation to the axisymmetric problem. In the next section, we summarize all these transitions in the wider range of $50 \leqslant \mathrm{Re}_Q \leqslant 300$.

As commented above, instabilities are spontaneously triggered in the numerical simulations from just numerical noise, without any external forcing, and they freely develop in space and time because of the numerical method used here. These instabilities inside the rotating pipe generate in the present work the required perturbations to trigger the instabilities in the swirling jet emerging from the rotating pipe. To have a preliminary idea of the expected range of values of S for the different transitions, Table I gives the critical swirl numbers (S_{ci}) for convective instabilities in a rotating Hagen–Poiseuille flow for the Reynolds numbers considered[21] and the critical swirl number for the appearance of axisymmetric vortex breakdown in axisymmetric numerical simulations S_{2Dvb}. These last axisymmetric results, which have been previously reported for different expansion ratios and inlet velocity profiles,[6] are obtained here with the same numerical method described above, but neglecting the variations with θ (a typical axisymmetric simulation takes just a few hours in our computer facilities). We shall see next that the axisymmetric vortex breakdown transition is substantially modified when the 3D flow is considered. All the critical swirl numbers for the different transitions found in this work as Re_Q is varied, together with those previously known ones given in Table I, are summarized in the last section, Fig. 24.

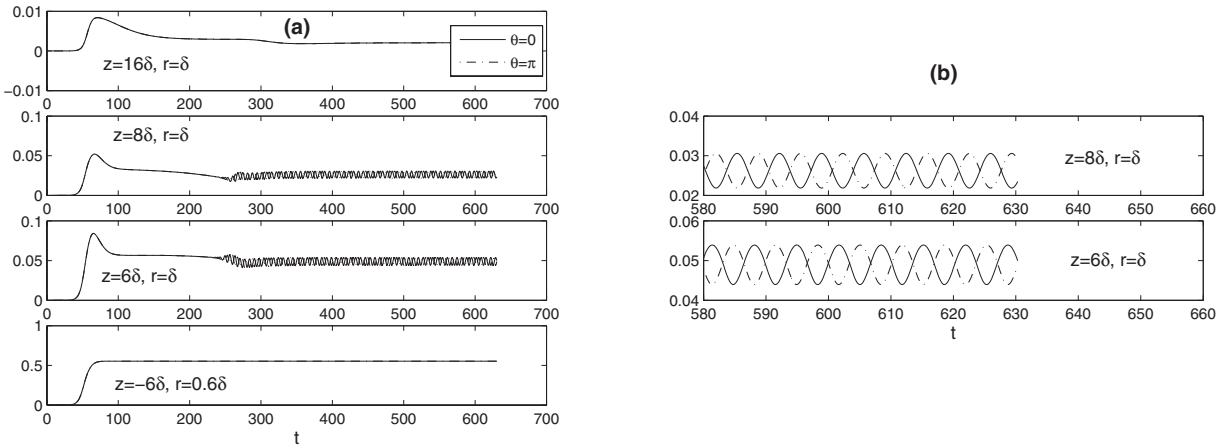

FIG. 7. Temporal evolution of v at $\theta=0$ (continuous lines) and at $\theta=\pi$ (dashed lines) in different meridional locations (z,r), as indicated in each subfigure. A detail of the oscillations is shown in (b). $\mathrm{Re}_Q=100$, $S=1$. Note that v is made dimensionless with V_c [see Eqs. (6) and (12)].

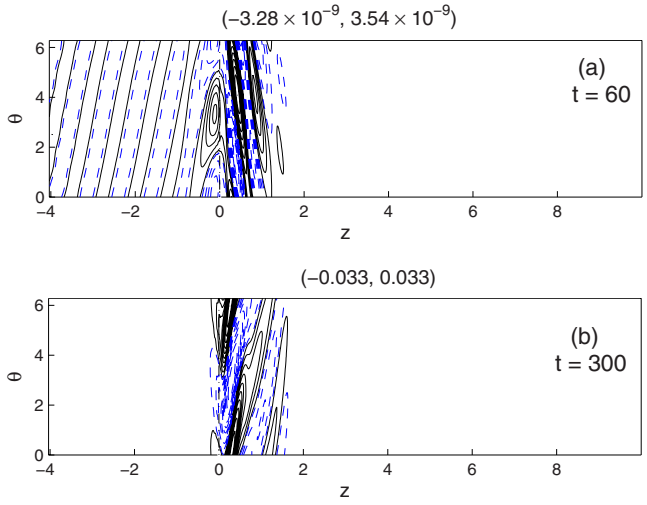

FIG. 8. (Color online) As in Fig. 3, but for $S=1$, and for two instants of time, as indicated in each subfigure. The interval of contour values plotted is indicated on the top.

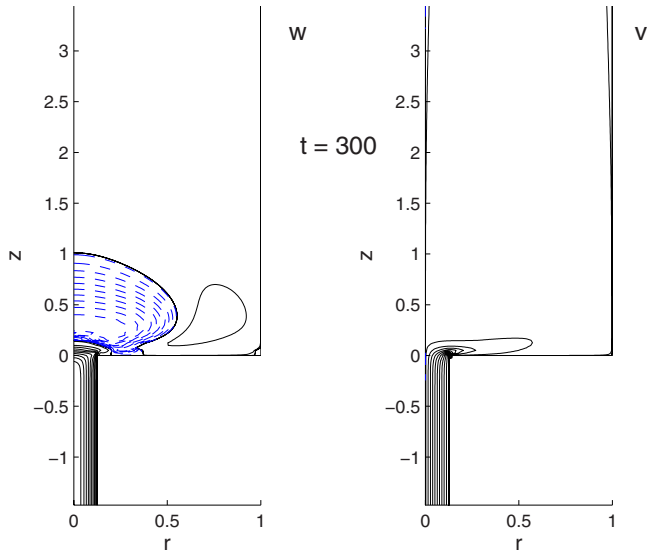

FIG. 9. (Color online) Contour lines of the axial velocity w and the azimuthal velocity v (as indicated) in the axial plane $\theta=0$ for a numerical simulation with $\mathrm{Re}_Q=100$ and $S=1.1$, but starting at $t=0$ with the final state at $S=1$ [see Fig. 6(a)].

A. $\mathrm{Re}_Q=100$

For $S<S_{\mathrm{ci}}(\mathrm{Re}_Q=100)\simeq 0.46$, the flow remains axisymmetric all the time, both inside the rotating pipe and in the swirling jet. For S slightly larger than S_{ci}, linear instabilities develop inside the rotating pipe in the form of traveling waves, leaving the pipe with the swirling jet and disappearing downstream as the jet expands. The amplitudes of these perturbations are so small throughout that the flow is basically axisymmetric. This behavior is documented in Figs. 2 and 3 for $S=0.5$ ($\mathrm{Re}_\theta=50$). Figure 2 shows that the flow is basically axisymmetric, both at $t=100$, when the mean flow is still developing, and at $t=800$, when the mean flow has reached a steady state long time ago (note that in this steady state, the swirling jet has practically no effect beyond $z\simeq 10=80\delta$). However, as shown in Fig. 3, there exist nonaxisymmetric waves with very small amplitude traveling in the pipe and in the emerging swirling jet. We plot the 3D traveling waves in the form of contour lines of the 3D azimuthal velocity perturbation, $v(r,\theta,z)-v(r,0,z)$, on the cylindrical surface $r=0.1$, which lies inside the rotating pipe (remember that the nondimensional radius of the pipe is $\delta=1/8=0.125$). The amplitude of these perturbations is very small, of the order of 10^{-9}, and they have grown in well organized traveling waves from round-off random numerical noise, which is of the order of 10^{-15}. For $z<0$ (rotating pipe), one observes traveling waves with azimuthal wavenumber $n=-1$, which correspond to the most unstable mode inside the rotating pipe for the present conditions.[21] It was shown in Ref. 15 that the wavelength and frequencies of these waves agree quite well with the predictions of the stability analysis. As these waves leave the rotating pipe ($z>0$), they are transformed into a very different train of traveling waves, with azimuthal wavenumber $n=+1$, which corresponds to the most unstable mode in a typical swirling jet for these values of the Reynolds number and swirl parameter,[22] though no linear stability analyses for the present configuration of an axisymmetric swirling jet emerging from a rotating pipe is available (to our knowledge) to check quantitatively our numerical wavelengths and frequencies. It must be noted that the definition of the sign of the azimuthal modes is in accordance with standard stability analyses [phase given by $\exp(ikz+in\theta)$, being k is the axial wavenumber],[21,22] where $n=-1$ means winding with the main flow (if $k>0$), while $n=+1$ corresponds to a counterwinding mode.[23] Comparing Figs. 2 and 3, one observes that the perturbation waves travel downstream until the swirling jet practically vanish at $z\simeq 10=80\delta$. The waves are better appreciated in the 3D visualization of Fig. 4.

When the swirl parameter increases, the behavior of the flow is qualitatively similar, as shown in Fig. 5 for $S=0.9$. Comparing this figure with Fig. 2, one observes that the increment of the rotation rate in the pipe makes the ensuing swirling jet more concentrated near the pipe exit (at the plotted instant $t=700$ the mean flow has well reached a steady state). The other quantitative difference is that the amplitude of the spiral traveling waves notably increases (by one order of magnitude, approximately), but not enough to be appreciated in the contour plot of Fig. 5, which remains basically axisymmetric.

The situation substantially changes for $S=1$, as it is shown in Figs. 6–8. The final flow is no longer axisymmetric: Helical traveling waves in the pipe now trigger new instabilities in the swirling jet producing waves whose amplitude increases by many orders of magnitude (see below), and their effects are perfectly visible in the contour lines of w and v on the axial plane $\theta=0$ plotted in Fig. 6(a). This is better appreciated in the contour plot for the azimuthal velocity, where it is seen that v does not vanish at the axis like in the axisymmetric case, but alternates between positive and negative values along it as a consequence of the traveling helical waves of finite amplitude. This swirling jet instability appears above a critical swirl $S_{3\mathrm{D}i}(\mathrm{Re}_Q)$, which is approximately 0.97 for the present case of $\mathrm{Re}_Q=100$.

The existence of these 3D waves is not the most impor-

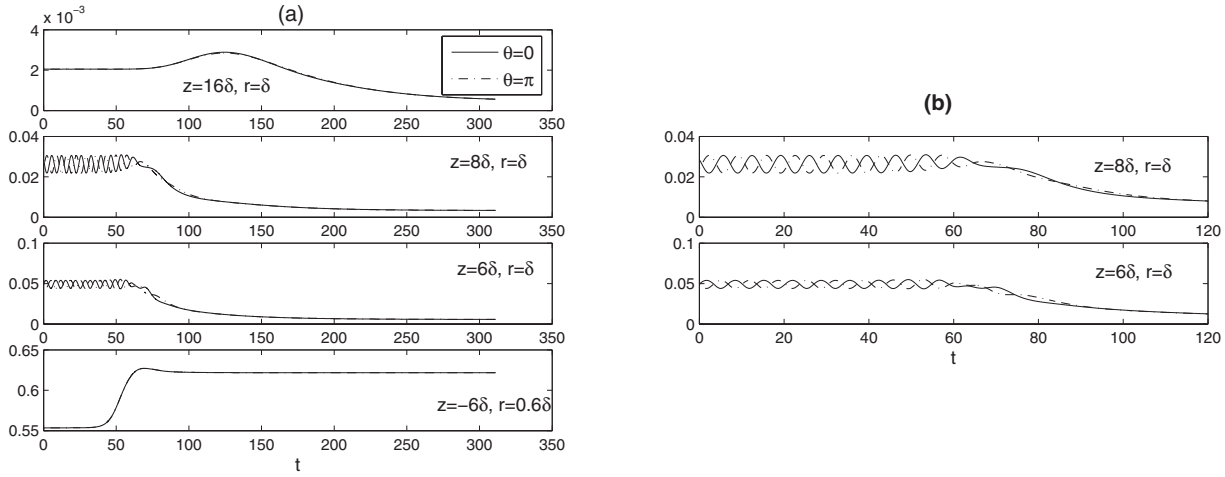

FIG. 10. As in Fig. 7, but for $S=1.1$, and starting at $t=0$ with the final solution for $S=1$.

tant qualitative difference with respect to the axisymmetric flow for the same conditions $\mathrm{Re}_Q=100$ and $S=1$, but it is the absence of vortex breakdown in the swirling jet, a phenomenon which is already present in the axisymmetric simulation for the same conditions (note in Table I that $S=1$ is larger than $S_{2\mathrm{Dvb}}$ for $\mathrm{Re}_Q=100$). In Fig. 6(b) we depict the result of the axisymmetric simulation for the same conditions and instant of time, clearly showing a region of recirculating flow, or vortex breakdown "bubble," on the axis, approximately between $z=1.3\simeq 10\delta$ and $z=2.5=20\delta$, in addition to other significant differences with the 3D flow. Thus, one of the main consequences of the 3D instabilities and the subsequent formation of nonlinear traveling waves in the swirling jet is the delay in the onset of vortex breakdown in the swirling jet, which for $\mathrm{Re}_Q=100$ and for the present expansion ratio takes place at $S=S_{3\mathrm{Dvb}}\simeq 1.0075$ (this difference between $S_{3\mathrm{Dvb}}$ and $S_{2\mathrm{Dvb}}$ notably increases with Re_Q; see below).

The formation and development of the nonaxisymmetric waves in this case $S=1$ are described in Figs. 7 and 8. Figure 7 shows the temporal evolution of the azimuthal velocity at $\theta=0$ and $\theta=\pi$ for different meridional locations (r,z). In the scale of the figure, the formation of the traveling waves is clear inside the swirling jet ($z=0.75=6\delta$ and $z=1=8\delta$) beyond $t\simeq 225$, though they are actually formed much earlier in time. Farther downstream ($z=2=16\delta$), the amplitude of the waves decays with the swirling jet, and they are not seen in the figure. Of course, traveling waves are present inside the pipe ($z=-0.75=-6\delta$) because they are initiated from centrifugal instabilities there, but their amplitude remains so small that are not observed in the scale of the figure. It is seen that inside the pipe a (quasi) steady state is reached much before 100 time units. However, Fig. 8(a) shows that at $t=60$ traveling waves are already present inside the rotating pipe ($z<0$), with azimuthal wave number $n=-1$, and in the swirling jet ($z>0$), with $n=1$, but their amplitudes are very small, of the order of 10^{-9} everywhere. Figure 8(b) shows that this initial mode $n=1$ in the swirling jet eventually disappears, emerging a new mode with $n=-1$ from the pipe exit, growing very fast in time inside the swirling jet, due to the new instability there, and reaching an amplitude of the order of 10^{-2} (it grows more than seven orders of magnitude between $t=60$ and $t=300$!). In contrast, the mode $n=-1$ inside the pipe has a much lesser growth rate and saturates at an amplitude of the order of 10^{-9}, this being the reason why it is not observed in Figs. 7 and 8(b).

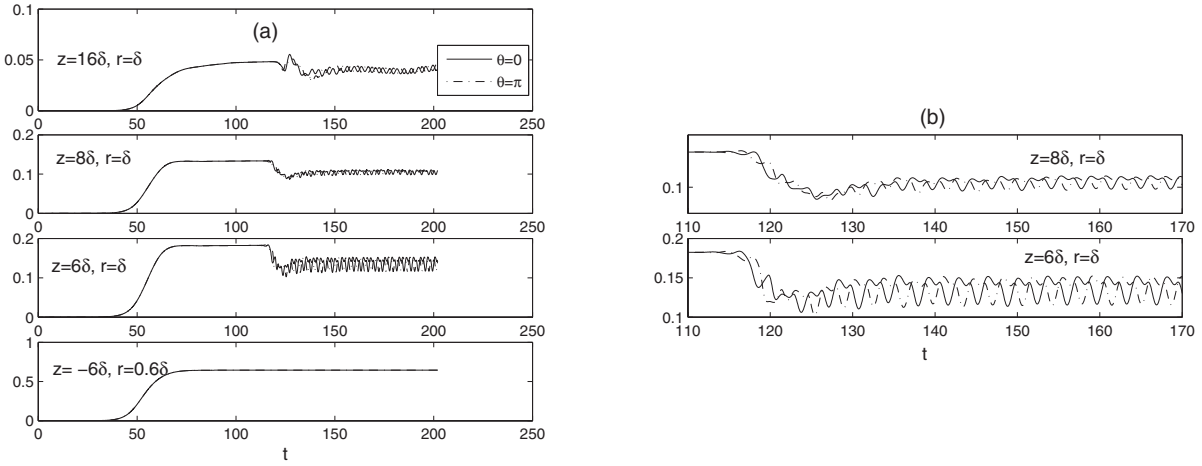

FIG. 11. As in Fig. 7, but for $\mathrm{Re}_Q=150$ and $S=0.9$.

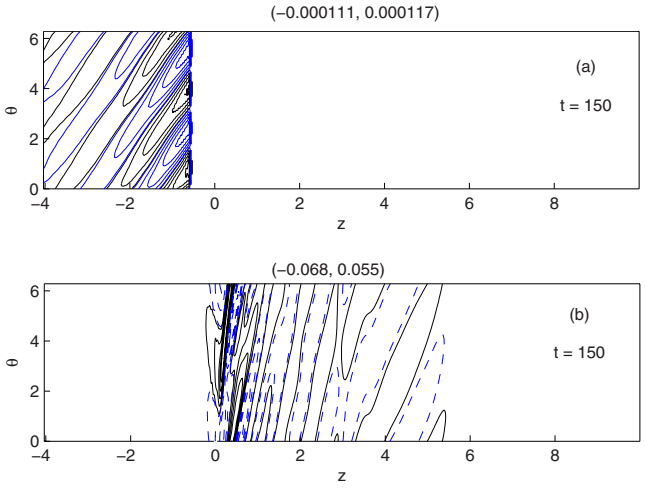

FIG. 12. (Color online) As in Fig. 3, but for $\mathrm{Re}_Q=150$ and $S=0.9$, and for $t=150$. The interval of contour values plotted are indicated on the top of each subfigure. Note that the amplitude of the waves inside the rotating pipe (a) is much smaller than in the swirling jet (b), but they have been separately plotted to show that $n=-2$ is the dominant mode inside the rotating pipe.

The above behavior of the flow remains until the swirl parameter reaches the critical value $S=S_{3\mathrm{Dvb}}$ for the appearance of vortex breakdown in the 3D swirling jet mentioned above (all the critical values of S commented on in this section are summarized in Sec. IV below as functions of Re_Q). Once this critical swirl is surpassed, the structure of the flow dramatically changes because the vortex breakdown bubble is almost axisymmetric, forcing the swirling jet to be also axisymmetric, dissipating the helical waves coming from the rotating pipe. This behavior can be appreciated in Figs. 9 and 10, where we plot the results of a 3D numerical simulation for $S=1.1$, but starting with initial conditions at $t=0$ corresponding to the final state reached for $S=1$ [Fig. 6(a)]. Figure 9 shows the final ($t=300$) state. The flow is clearly nonaxisymmetric at $t=0$ [Fig. 6(a)], but once the breakdown bubble is formed on the axis of the swirling jet, the flow becomes practically axisymmetric. This evolution is better appreciated in Fig. 10. Initially, the flow contains nonlinear traveling waves in the jet, which disappear beyond $t=50$, approximately due to the formation of the breakdown bubble at the axis. At $t=300$, the flow is practically axisymmetric everywhere. In fact, infinitesimal traveling waves are present inside the rotating pipe, that are not visualized in the scale of the figures, but they are dissipated by the huge breakdown bubble at the pipe exit (see Fig. 9), where the *local* Reynolds number becomes much smaller.

B. $\mathrm{Re}_Q=150$

This case is partially similar to the previous one. The flow remains axisymmetric for $S<S_{\mathrm{ci}}(\mathrm{Re}_Q=150)\simeq 0.20$. For $S>S_{\mathrm{ci}}$, nonaxisymmetric instabilities with azimuthal wave number $n=-1$ develop inside the rotating pipe in the form of traveling waves, which are then amplified in the jet and transformed into traveling waves with $n=+1$. For S slightly larger than S_{ci}, these waves have very small amplitude, like in the case $\mathrm{Re}_Q=100$, and the mean flow is basically axisymmetric. However, the amplitude of the waves dramatically grows in the swirling jet for $S\geqslant S_{3\mathrm{D}i}(\mathrm{Re}_Q=150)\simeq 0.80$, becoming of the order of 10^{-2}.

The main difference with the case $\mathrm{Re}_Q=100$ is that the waves developing in the swirling jet for $S\geqslant S_{3\mathrm{D}i}$ have azimuthal wave number $n=-2$, which is now the most unstable mode, replacing the waves with $n=\pm 1$ of the previous case. This is illustrated in Figs. 11 and 12 for $S=0.9$. Traveling waves with $n=-1$ in the pipe and $n=+1$ in the jet are already formed at $t=50$, when the Reynolds number of the flow has not reached yet its final value $\mathrm{Re}_Q=150$, but their amplitude is so small that they cannot be appreciated in the time evolution plot of Fig. 11. As in the case $\mathrm{Re}_Q=100$, the azimuthal wave number of the successive traveling waves in the jet is transformed into $n=-1$, amplifying those coming from the pipe. At $t=100$, approximately, the dominant instability in the pipe becomes $n=-2$ [compare the contour lines in Fig. 12(a) with those in Fig. 3], which is also amplified in the jet, and this is the dominant mode amplified in the swirling jet that becomes "visible" in the time evolution plot depicted in Fig. 11 for $t>110$, approximately. At $t=150$, the amplitude of the waves has already become saturated, with an amplitude in the jet (at $z=0.75=6\delta$) which is almost one-third of

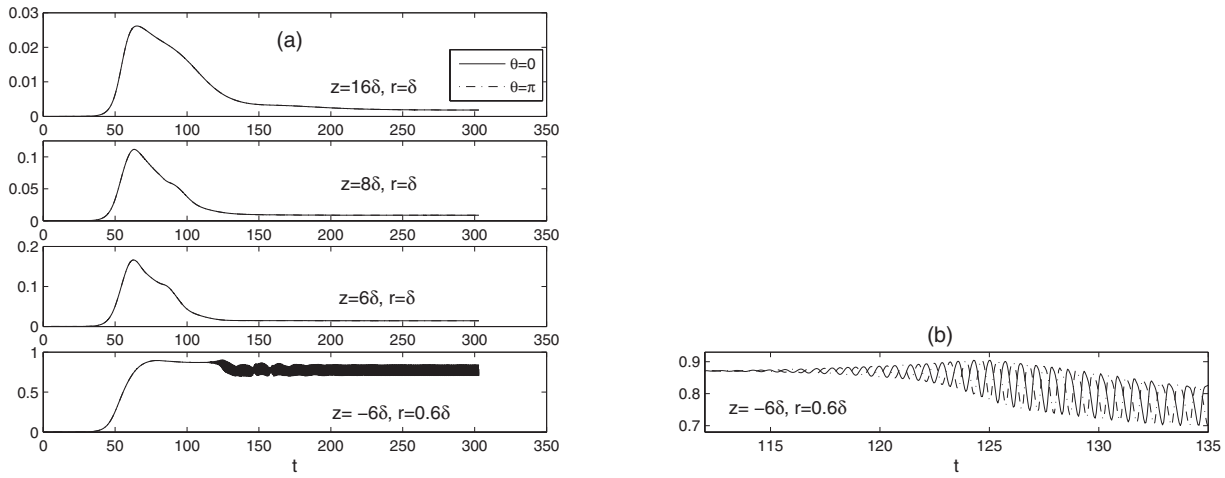

FIG. 13. As in Fig. 7, but for $\mathrm{Re}_Q=150$ and $S=1.1$.

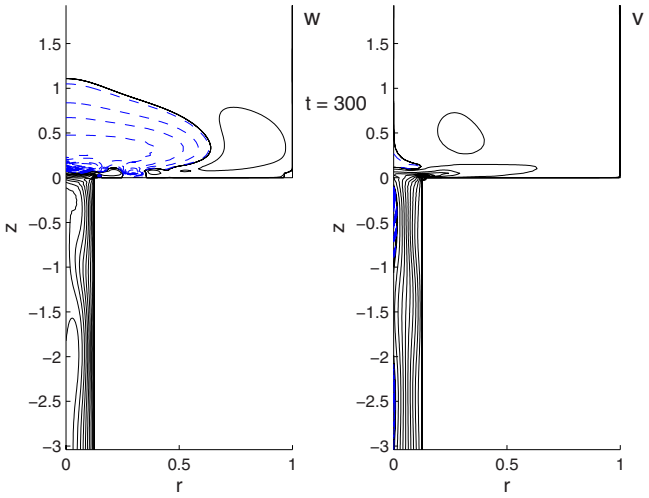

FIG. 14. (Color online) Detail near the pipe exit of the contour lines of w and v (as indicated) in the axial plane $\theta=0$ for $\mathrm{Re}_Q=150$, $S=1.1$, and $t=300$. Contour lines as described in the caption of Fig. 2, with w between −0.148 and 1.228 and v between −0.158 and 1.367.

the mean flow. The structure of these waves with $n=-2$ at $t=150$ is shown in Fig. 12(b). They are concentrated in the swirling jet at the pipe exit, decaying far downstream. Note that the amplitude of the waves inside the rotating pipe, which trigger the swirling jet instability, is almost three orders of magnitude smaller than the amplitude of the swirling jet waves.

At $S=S_{2\mathrm{Dvb}}(\mathrm{Re}_Q=150)\simeq 0.9675$, the axisymmetric flow undergoes vortex breakdown. But, like in the former case with $\mathrm{Re}_Q=100$, the instabilities in the 3D flow delay the formation of vortex breakdown in the swirling jet until $S=S_{3\mathrm{Dvb}}(\mathrm{Re}_Q)\simeq 1.065$. Once a breakdown bubble is formed for $S>S_{3\mathrm{Dvb}}$, the jet becomes again basically axisymmetric, damping the traveling waves coming from the pipe. This is illustrated for $S=1.1$ in Figs. 13–15. Figures 14 and 15 show how the traveling waves in the pipe, which are very intense for this value of the swirl $S=1.1$ [see also Fig. 13(b)], are dissipated by the vortex breakdown bubble formed just downstream the pipe exit. The flow in the jet is not exactly axisymmetric, but the amplitude of the residual traveling waves is so small that they cannot be appreciated in the time plots depicted in Fig. 13(a). Finally, for $S>1.1$, the structure of the flow remains qualitatively similar to this one, with the size of the breakdown bubble increasing with S (the maximum value of S used in our computations has been $S=1.6$).

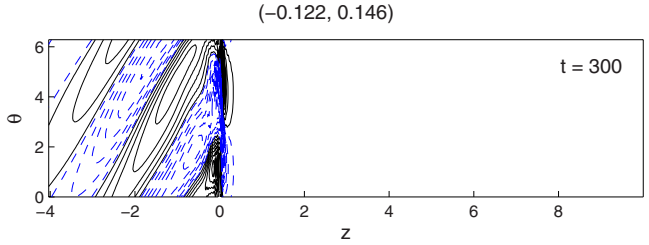

FIG. 15. (Color online) As in Fig. 3, but for $\mathrm{Re}_Q=150$ and $S=1.1$, and for $t=300$. The interval of contour values plotted is indicated on the top.

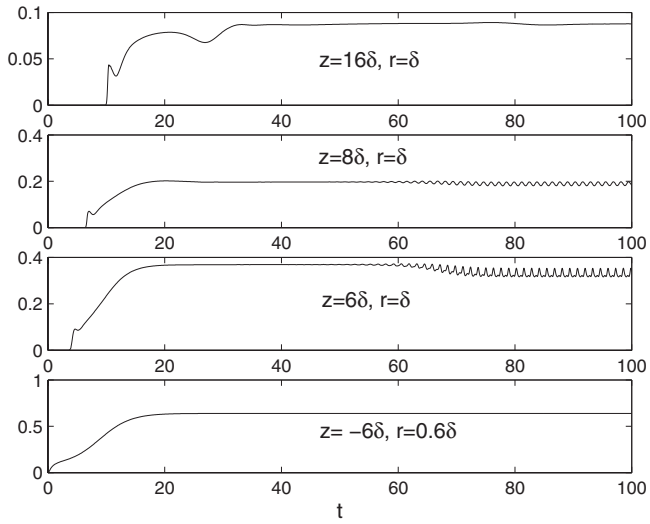

FIG. 16. Temporal evolution in the axisymmetric simulation of v at different locations (z,r), as indicated in each subfigure. $\mathrm{Re}=200$, $S=0.95$.

C. $\mathrm{Re}_Q=200$

The main difference of this case in relation to the previous ones is the appearance of axisymmetric instabilities in the swirling jet in the results of the axisymmetric (2D) simulations above a critical swirl S_{2Di}, which for $\mathrm{Re}_Q=200$ is $S_{2Di}\simeq 0.912$. These critical swirl parameters are also summarized as functions of Re_Q in the last section (Fig. 24 below), along with the remaining critical swirl parameters discussed in the present work. It is observed in that diagram that this axisymmetric instability appears also above a critical Reynolds number, $\mathrm{Re}_Q\gtrsim 188$, in the present configuration. This oscillatory behavior above a threshold Reynolds number, when the swirl number is also larger than a critical value, has been previously observed in axisymmetric numerical simulations with a different swirling jet at the inlet and different aspect ratios of the sudden expansion.[6]

Figures 16 and 17 show the results from an axisymmet-

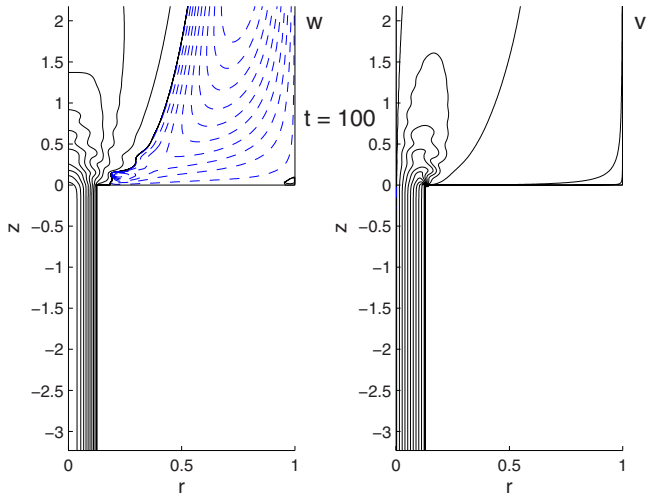

FIG. 17. (Color online) Detail near the pipe exit of the contour lines of w and v (as indicated) for the flow in the axisymmetric simulation with $\mathrm{Re}_Q=200$ and $S=0.95$ at $t=100$. The contour lines of w range between −0.023 and 1.111 and those of v between 0 and 1.050.

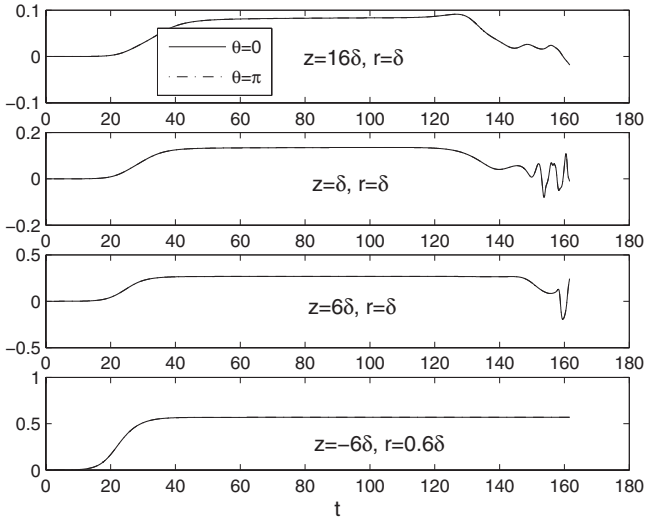

FIG. 18. As in Fig. 7, but for $\mathrm{Re}_Q=200$ and $S=0.7$.

ric numerical simulation for $S=0.95>S_{2Di}\simeq 0.912$. The oscillatory behavior is clear at the rotating pipe exit and the initial stages of the swirling jet. However, this axisymmetric instability does not appear in the 3D simulations because the flows inside the rotating pipe and in the swirling jet become unstable to nonaxisymmetric perturbations at swirl numbers much lower than S_{2Di}. In particular, the rotating pipe flow becomes unstable to helical perturbations with $n=-1$ at $S_{ci}(\mathrm{Re}_Q=200)\simeq 0.14$ (see Table I or Fig. 24 below). These perturbations become unstable and grow very fast in the swirling jet for $S>S_{3Di}(\mathrm{Re}_Q=200)\simeq 0.695$. Thus, when $S=0.7$ (see Figs. 18–20), the flow is completely transformed by the nonaxisymmetric instabilities in relation to the axisymmetric simulation. As in the previous values of Re_Q, the instabilities in the swirling jet for relatively low values of S are triggered by the instabilities in the rotating pipe. This is also the case for $S=0.7$ at the initial stages of the flow starting from rest. However, as time goes on, the main instabilities are produced inside the swirling jet. Thus, Fig. 18 shows that a strong instability develops in the jet for $t\gtrsim 120$, while

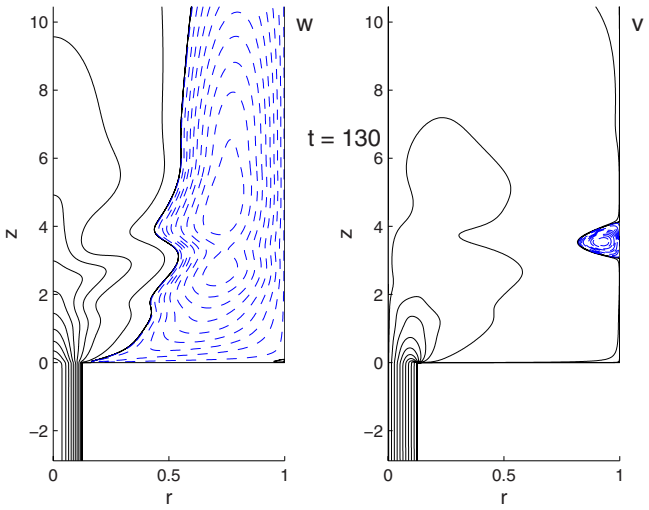

FIG. 19. (Color online) As in Fig. 2 but for $\mathrm{Re}_Q=200$, $S=0.7$, and $t=130$. w ranges between −0.033 and 1.347 and v between −0.00071 and 0.936.

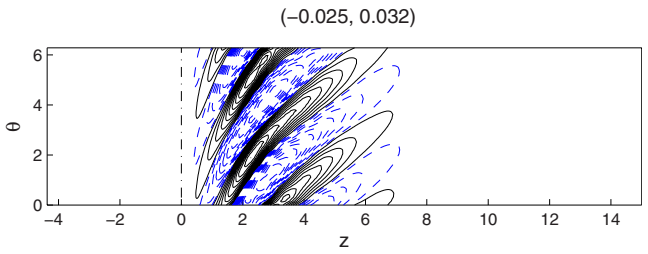

FIG. 20. (Color online) As in Fig. 3, for $\mathrm{Re}_Q=200$, $S=0.7$, and $t=130$. The interval of contour values plotted is indicated on the top.

the amplitudes of the traveling waves inside the pipe remain small and cannot be appreciated in that figure. This instability corresponds to $n=-2$ (Fig. 20), and for $t=130$ has completely transformed the basic axisymmetric flow (Fig. 19).

For this Reynolds number, we find that $\mathrm{Re}_{2Dvb}\simeq 1.005$ and $\mathrm{Re}_{3Dvb}\simeq 1.100$ (see also Fig. 24 below). Again, for $\mathrm{Re}>\mathrm{Re}_{3Dvb}$, the swirling jet flow becomes almost axisymmetric, though the incoming pipe flow is clearly nonaxisymmetric (see Figs. 21–23 for $S=1.5$). As in the previous cases, the recirculating flow region at the axis produced by vortex breakdown in the jet dissipates the nonaxisymmetric traveling waves coming from the rotating pipe. Note in Fig. 23 that these waves have an azimuthal wavenumber $n=-2$, which are the most unstable ones in the rotating pipe for these values of Re_Q and S.[21]

IV. SUMMARY OF THE RESULTS AND CONCLUSIONS

Figure 24 summarizes all the different transitions in the present flow on a plane Re_Q-S, in the range of $50\leqslant \mathrm{Re}_Q \leqslant 300$. These transitions have been discussed above for the cases $\mathrm{Re}_Q=100$, 150, and 200. Also included is the critical swirl $S_{ci}(\mathrm{Re}_Q)$ for instability of rotating Hagen–Poiseuille flow. Below this curve the flow is axisymmetric everywhere, both in the rotating pipe and in the discharging swirling jet. The asymptote $S\to\infty$ of this curve, $\mathrm{Re}_Q=\mathrm{Re}_{Qci}\simeq 82.9$, first obtained by Pedley,[24] marks the minimum value of the Reynolds number at which nonaxisymmetric instabilities may develop in the rotating pipe; for $\mathrm{Re}_Q<\mathrm{Re}_{Qci}$ the flow remains axisymmetric, no matter how large is S.

Even for these low values of the Reynolds number, the swirling jet undergoes (axisymmetric) vortex breakdown if the swirl parameter is larger than S_{2Dvb}, which coincides with S_{3Dvb} for these low values of Re_Q. In fact, there exists a critical Reynolds number Re_{Q3D}, which for the present expansion ratio is $\mathrm{Re}_{Q3D}\simeq 98$, below which vortex breakdown in the swirling jet is basically an axisymmetric phenomenon: although nonaxisymmetric instabilities develop in the rotating pipe for $S>S_{ci}(\mathrm{Re}_Q)$, producing traveling waves that are enhanced and transformed in the swirling jet, their amplitudes remain so small that the flow is basically axisymmetric and $S_{3Dvb}\simeq S_{2Dvb}$. However, at $\mathrm{Re}_Q=\mathrm{Re}_{Q3D}$, there exists a bifurcation in the jet flow (marked with a square in Fig. 24), with a lower branch $S_{3Di}(\mathrm{Re}_Q)$ at which the swirling jet itself becomes unstable to nonaxisymmetric perturbations and an upper branch $S_{3Dvb}(\mathrm{Re}_Q)$ marking the onset of vortex breakdown in the swirling jet. Thus, for $\mathrm{Re}_Q>\mathrm{Re}_{Q3D}$, one has the following regimes as the swirl parameter is increased.

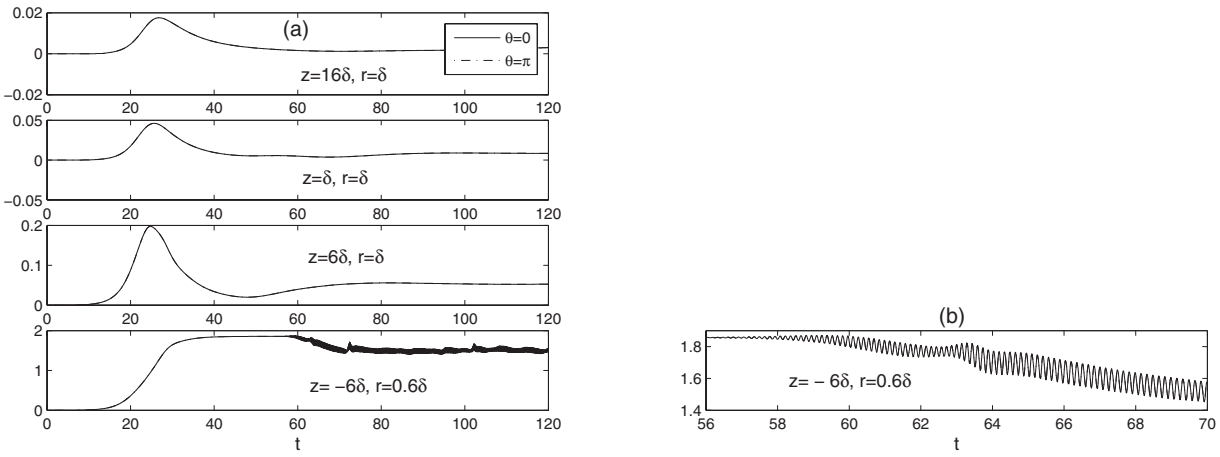

FIG. 21. As in Fig. 7, but for $\mathrm{Re}_Q=200$ and $S=1.5$.

For $S<S_{\mathrm{ci}}$ the flow is axisymmetric everywhere; for $S_{\mathrm{ci}}<S<S_{3\mathrm{D}i}$, nonaxisymmetric instabilities in the rotating pipe generate traveling waves that develop in the jet, but their amplitudes remain small; for $S_{3\mathrm{D}i}<S<S_{3\mathrm{Dvb}}$, these nonaxisymmetric traveling waves coming from the pipe trigger new nonaxisymmetric instabilities in the swirling jet which transform the structure of the flow; finally, at $S=S_{3\mathrm{Dvb}}$ vortex breakdown occurs in the jet and a bubble of recirculating flow is formed at the rotating pipe exit which increases in size with S. One of the main conclusions of this work is that once the breakdown bubble is formed when $S>S_{3\mathrm{Dvb}}(\mathrm{Re}_Q)$, the swirling jet becomes again almost axisymmetric, with the breakdown bubble acting as a "buffer" of the nonaxisymmetric flow coming from the rotating pipe (see, e.g., Fig. 23). This picture of the different flow regimes remains basically the same for all the Reynolds numbers larger than $\mathrm{Re}_{Q3\mathrm{D}}$ considered in this work (up to $\mathrm{Re}_Q=300$), with the only qualitative differences related to the particular azimuthal mode that becomes the most unstable one in the swirling jet and in the rotating pipe. It must be noted that all the nonlinear instabilities observed here in the swirling jet for $S>S_{3\mathrm{D}i}$ correspond to $n<0$ ($n=-1$ or $n=-2$, depending on Re_Q); i.e., they form traveling waves cowinding with the main flow, in qualitative agreement with some previous experimental studies of swirling jets.[23,25]

Figure 24 also shows with dashed lines the transitions taking place in an strictly axisymmetric flow, obtained here with the same numerical code but dropping all the azimuthal derivatives of the flow properties. The structure is somewhat similar to that previously described, with a bifurcation of the critical swirl for axisymmetric vortex breakdown $S_{2\mathrm{Dvb}}(\mathrm{Re}_Q)$ at $\mathrm{Re}_Q=\mathrm{Re}_{Q2\mathrm{D}}\simeq 188$. The lower branch $S_{2\mathrm{D}i}(\mathrm{Re}_Q)$ starting at this Reynolds number marks the onset of axisymmetric instability in the swirling jet for $S>S_{2\mathrm{D}i}$, which generates axisymmetric oscillations in the jet that are damped by the 2D vortex breakdown when $S=S_{2\mathrm{Dvb}}$. Obviously, these axisymmetric instabilities are not observed in the real 3D flows because nonaxisymmetric instabilities transform the axisymmetric flow at values of the swirl parameter much lower than $S_{2\mathrm{D}i}$. Another important finding of this work is that these nonaxisymmetric instabilities delay the appearance of the vortex breakdown phenomenon in the swirling jet to values of the swirl parameter significantly larger than those found in the axisymmetric simulations. We observe in Fig. 24 that $S_{3\mathrm{Dvb}}>S_{2\mathrm{Dvb}}$ for $\mathrm{Re}_Q>\mathrm{Re}_{Q3\mathrm{D}}\simeq 98$. As commented on above, for $\mathrm{Re}_Q<\mathrm{Re}_{Q3\mathrm{D}}$ the flow is practically axisymmetric (it is actually axisymmetric for $S<S_{\mathrm{ci}}$) and the two curves, $S_{3\mathrm{Dvb}}(\mathrm{Re}_Q)$ and $S_{2\mathrm{Dvb}}(\mathrm{Re}_Q)$, practically coincide.

Finally, it is worth to mention that, for the moderately large Reynolds numbers considered here ($\mathrm{Re}_Q\leqslant 300$), we have not observed the instabilities inside the breakdown bubble that trigger the helical form of vortex breakdown reported in the numerical simulations of Refs. 11, 13, and 14 for a quite different type of swirling jet and for sufficiently large swirl and Reynolds numbers. Probably, these instabilities will also exist in the swirling jet considered here for high values of S if Re_Q is larger than another critical value which in the present problem is larger than 300. But the cost of the numerical computations increases so fast with Re_Q, that going beyond $\mathrm{Re}_Q=300$ with our present computer facilities becomes prohibitive. However, we think that the richness of the different transitions and flow structures found in this

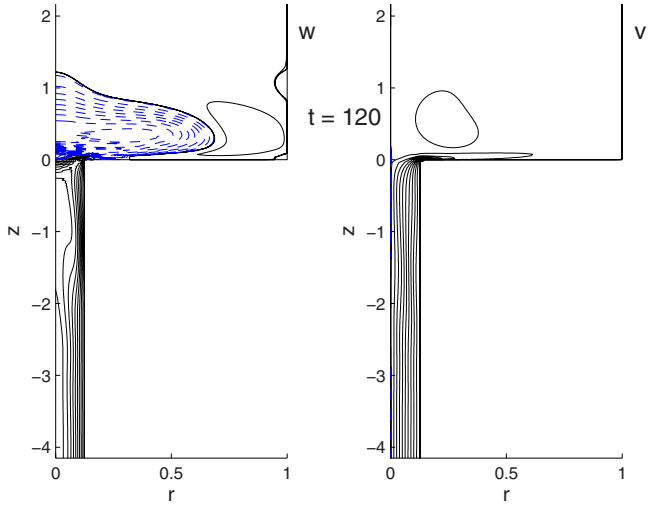

FIG. 22. (Color online) As in Fig. 14 but for $\mathrm{Re}_Q=200$, $S=1.5$, and for $t=120$. w ranges between −0.11 and 1.77 and v between −0.010 and 2.59.

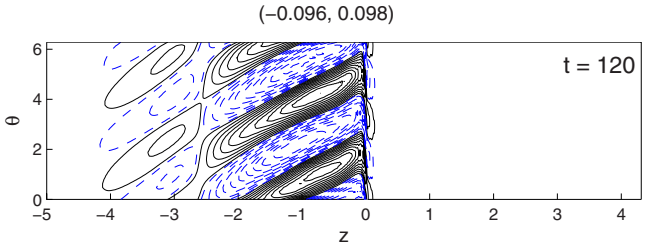

FIG. 23. (Color online) As in Fig. 3, but for $\mathrm{Re}_Q=200$ and $S=1.5$, and for $t=120$. The interval of contour values plotted is indicated on the top.

work for $\mathrm{Re}_Q \leqslant 300$, the precise characterization and discussion of these transitions, and their possible relevance for technological swirl devices, justify the present numerical study, leaving for future numerical and, especially, experimental works the study of higher Reynolds numbers.

ACKNOWLEDGMENTS

This work has been supported by the Ministerio de Educación y Ciencia of Spain (Grant Nos. FIS2004-00538, DPI2005-08654-C04-01, and TRA2006-15015). The numerical computations were performed in the computer facility "Taylor," at the ETSII (U. Málaga), and in the computer facilities at the SAIT (U.P. Cartagena).

APPENDIX: CONVERGENCE STUDY OF THE NUMERICAL METHOD

Here, we report a convergence study of the numerical method to asses the accuracy of the numerical results given in the main text. Table II summarizes the different meshes used in this convergence analysis. In all the computations we use a time step $\delta t=5\times10^{-4}$. Mesh 2 is the one used in all the numerical simulations reported in this paper. We are particularly interested in the influence of the number of azimuthal nodes n_θ in the results, so that meshes 3 and 4 have the same number of meridional nodes $n_r\times n_z$ than mesh 2 but increasing values of n_θ. The numerical results are checked against the results obtained from a very fine grid (mesh 5), with double values of n_r and n_z, and the maximum value of n_θ (note the huge number of nodes of this mesh, six times larger than in mesh 2). Mesh 1 is a coarser grid, with half n_r and n_z, and a smaller value of n_θ.

TABLE II. Different meshes used in the convergence study. Mesh 2 is the one used in all the numerical simulations reported in the paper.

Mesh	n_r	n_z	n_θ	Number of nodes
1	103	189	8	115 905
2	205	377	10	583 657
3	205	377	12	700 313
4	205	377	14	816 969
5	409	753	14	3 280 310

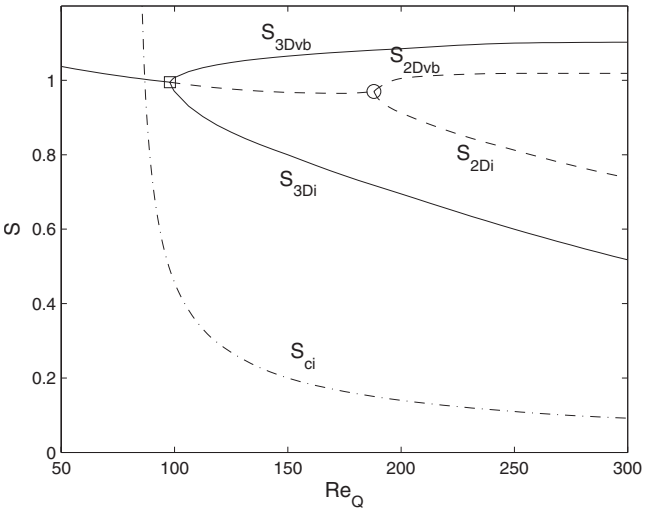

FIG. 24. Critical swirl numbers as functions of the Reynolds number for the different transitions considered in this work with an expansion ratio $\delta^{-1}=8$. With continuous lines, we plot transitions in the 3D swirling jet: Nonaxisymmetric instabilities (S_{3Di}) and vortex breakdown (S_{3Dvb}). With dashed lines, transitions in the axisymmetric simulations: Axisymmetric instabilities (S_{2Di}) and vortex breakdown (S_{2Dvb}). With a square is marked the bifurcation corresponding to $\mathrm{Re}_{Q3D}\simeq 98$ (with $S\simeq 0.995$), while that corresponding to $\mathrm{Re}_{Q2D}\simeq 188$ is marked with a circle (with $S\simeq 0.970$). Finally, with dash-and-dot lines we plot the critical swirl S_{ci} for convective instabilities in the rotating Hagen–Poiseuille flow (Ref. 21).

where ϕ_i is some physical quantity computed with mesh i. In particular, we have used the axial (w) and azimuthal (v) velocity components at two different points, one inside the rotating pipe (point 1, corresponding to $r=0.6\delta$, $\theta=0$, and $z=-6\delta$), and the other one in the swirling jet (point 2, corresponding to $r=\delta$, $\theta=0$, and $z=6\delta$), at the instant $t=100$ for $\mathrm{Re}_Q=100$ and $S=1$. It is observed that inside the pipe (point 1) the relative errors with mesh 2 are $O(10^{-8})$, while in the swirling jet they are somewhat larger due to the

$$\mathrm{error}=\left|\frac{\phi_i-\phi_5}{\phi_5}\right|,\quad i=1,2,3,4, \tag{A1}$$

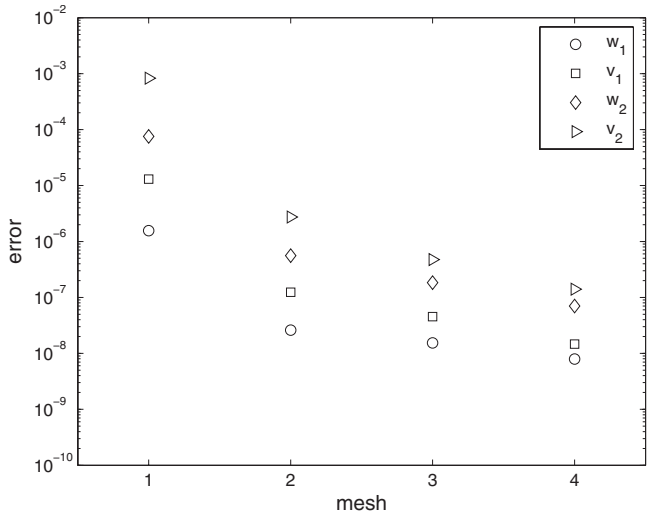

FIG. 25. Relative errors given by Eq. (A1) from the different meshes described in Table II for $\mathrm{Re}_Q=100$ and $S=1$ at $t=100$. (w_1,v_1) is computed at $(r=0.6\delta,\theta=0,z=-6\delta)$ and (w_2,v_2) at $(r=\delta,\theta=0,z=6\delta)$.

fact that the nodes are concentrated inside the rotating pipe and just at the rotating pipe exit. The important thing is that the accuracy of the results from mesh 2 is not very much improved when using finer grids, this being the reason why we opted for this mesh as a compromise between accurate results and reasonable computation time. This is so because the spatial resolutions in meshes 2–5 are sufficiently high for the relative errors to be mostly controlled by the time step [remember that the numerical method is second order in time and $\delta t = O(10^{-4})$]. The relative errors for mesh 1 are much larger and are controlled by the coarser spatial grid.

[1] M. Escudier, "Confined vortices in flow machinery," Annu. Rev. Fluid Mech. **19**, 27 (1987).
[2] A. H. Lefebvre, *Gas Turbine Combustion*, 2nd ed. (Taylor and Francis, New York, 1999).
[3] J. Ji and J. P. Gore, "Flow structure in lean premixed swirling combustion," Proc. Combust. Inst. **29**, 861 (2002).
[4] A. Revuelta, A. L. Sánchez, and A. Liñán, "Confined swirling jets with large expansion ratios," J. Fluid Mech. **508**, 89 (2004).
[5] A. Revuelta, A. L. Sánchez, and A. Liñán, "The quasi-cylindrical description of submerged laminar swirling jets," Phys. Fluids **16**, 848 (2004).
[6] A. Revuelta, "On the axisymmetric vortex breakdown of a swirling jet entering a sudden expansion pipe," Phys. Fluids **16**, 3495 (2004).
[7] P. Beran and F. Culik, "The role of nonuniqueness in the development of vortex breakdown in tubes," J. Fluid Mech. **242**, 491 (1992).
[8] J. M. Lopez, "On the bifurcation structure of axisymmetric vortex breakdown in a constricted pipe," Phys. Fluids **6**, 3683 (1994).
[9] S. Wang and Z. Rusak, "The effect of slight viscosity on near-critical swirling flows," Phys. Fluids **9**, 1914 (1997).
[10] Z. Rusak, K. P. Judd, and S. Wang, "The effect of small pipe divergence on near-critical swirling flows," Phys. Fluids **9**, 2273 (1997).
[11] M. R. Ruith, P. Chen, E. Meiburg, and T. Maxworhy, "Three-dimensional vortex breakdown in swirling jets and wakes: direct numerical simulation," J. Fluid Mech. **486**, 331 (2003).
[12] W. Grabowski and S. Berger, "Solutions of the Navier-Stokes equations for vortex breakdown," J. Fluid Mech. **75**, 525 (1974).
[13] M. A. Herrada and R. Fernandez-Feria, "On the development of 3D vortex breakdown in cylindrical regions," Phys. Fluids **18**, 084105 (2006).
[14] F. Gallaire, M. R. Ruith, E. Meiburg, J.-M. Chomaz, and P. Huerre, "Spiral vortex breakdown as a global mode," J. Fluid Mech. **549**, 71 (2006).
[15] E. Sanmiguel-Rojas and R. Fernandez-Feria, "Nonlinear waves in the pressure driven flow in a finite rotating pipe," Phys. Fluids **17**, 014104 (2005).
[16] L. Facciolo and P. H. Alfredsson, "The counter-rotating core of a swirling turbulent jet issued from a rotating pipe flow," Phys. Fluids **16**, L71 (2004).
[17] L. Facciolo, N. Tillmark, A. Talamelli, and P. H. Alfredsson, "A study of swirling turbulent pipe and jet flows," Phys. Fluids **19**, 035105 (2007).
[18] R. Fernandez-Feria and E. Sanmiguel-Rojas, "An explicit projection method for solving incompressible flows driven by a pressure difference," Comput. Fluids **33**, 463 (2004).
[19] E. Sanmiguel-Rojas, J. Ortega-Casanova, C. del Pino, and R. Fernandez-Feria, "A Cartesian grid finite-difference method for 2D incompressible viscous flows in irregular geometries," J. Comput. Phys. **204**, 302 (2005).
[20] P. A. Mackrodt, "Stability of Hagen-Poiseuille flow with superimposed rigid rotation," J. Fluid Mech. **73**, 153 (1976).
[21] R. Fernandez-Feria and C. del Pino, "The onset of absolute instability of rotating Hagen-Poiseuille flow: A spatial stability analysis," Phys. Fluids **14**, 3087 (2002).
[22] E. W. Mayer and K. G. Powell, "Viscous and inviscid instabilities of a trailing vortex," J. Fluid Mech. **245**, 91 (1992).
[23] F. Gallaire and J.-M. Chomaz, "Mode selection in swirling jets: an experimentally based instability analysis," J. Fluid Mech. **494**, 223 (2003).
[24] T. J. Pedley, "On the instability of viscous flow in a rapidly rotating pipe," J. Fluid Mech. **35**, 97 (1969).
[25] P. Billant, J.-M. Chomaz, and P. Huerre, "Experimental study of vortex breakdown in swirling jets," J. Fluid Mech. **376**, 183 (1998).